

DESIGN OF A NEW TEST RIG TO INVESTIGATE TRANSONIC EXTERNAL FAN COWL SEPARATION

K. Sabnis ^{(1) *}, L. Boscagli ⁽²⁾, A. Swarthout ⁽²⁾, H. Babinsky ⁽¹⁾, D. MacManus ⁽²⁾ and C. Sheaf ⁽³⁾

⁽¹⁾ Department of Engineering, University of Cambridge, Cambridge, CB2 1PZ, UK

⁽²⁾ Centre for Propulsion Engineering, Cranfield University, Cranfield, MK43 0AL, UK

⁽³⁾ Installation Aerodynamics, Rolls-Royce plc, Derby, DE24 8BJ, UK

* Corresponding author: ks648@cam.ac.uk

ABSTRACT

Ultra high-bypass ratio engines, which show considerable promise in reducing the environmental impact of commercial aviation, generally adopt slim fan cowl profiles. These geometries can be more sensitive to separation on the external surfaces in engine windmilling conditions during take-off climb out or during cruise. This paper describes the development of a two-dimensional wind tunnel rig which can accurately replicate the separation mechanisms experienced by real aero-engine nacelles. This design process highlights the importance of considering factors such as Reynolds-number effects, tunnel-wall effects, the two-dimensional nature of the rig, and the tunnel boundary layers.

1. INTRODUCTION

There is a pressing need to allow for sustainable growth of the civil aviation industry by reducing the environmental impact of commercial aircraft. This requirement has led to the European Commission setting the aviation sector challenging targets under the FlightPath 2050 vision, namely to reduce fuel consumption by 75% and perceived noise by 65% before 2050 [1].

A promising way to achieve these goals with current technology involves improving the propulsive efficiency of aircraft engines by increasing the engine bypass ratio. In particular, ultra high-bypass ratio (UHBR) engines, allow considerable performance improvements towards achieving the required fuel burn reductions. These UHBR engines require significantly larger fans, which require the engine nacelles to also be increased in cross-section. However, if the nacelles were also proportionally longer there would be a corresponding increase in drag. To avoid this detrimental effect, novel UHBR nacelles

need to be more compact by minimising both thickness and length while satisfying aerodynamic design requirements [2, 3].

Nacelle design is typically optimised for cruise operating conditions. However, the compact nature of UHBR nacelles necessarily requires more aggressive curvature at their leading edge, which can be problematic in certain off-design scenarios, such as engine windmilling conditions during take-off climb out or cruise. In these situations, the highly-curved geometry can cause flow separation on the external fan cowl surface [4], resulting in a considerable, negative impact on aircraft performance.

However, despite the prevalence and importance of these off-design situations, the separation behaviour on external nacelle surfaces remains poorly understood due to a lack of in-depth knowledge about the underlying flow physics. Furthermore, the flow field is not reliably computed by the Reynolds-averaged Navier–Stokes (RANS) methods typically used in industry, which is particularly problematic for nacelle designers. These difficulties are compounded by a notable lack of high-quality experimental reference data which can be used to validate relevant numerical methods. The current study aims to address this lack of understanding by designing a novel experimental set-up to investigate this flow problem.

2. DEFINITION OF FLOW PROBLEMS

The two specific flight regimes where external fan cowl separation is expected to be problematic are at engine shutdown during the take-off climb out phase (or “end-of-runway windmilling”) and during the cruise phase (or “diversion windmilling”) of flight.

The key parameters which are expected to govern the flow behaviour in these scenarios are: the incidence angle (α), the incoming freestream Mach number (M_∞), the

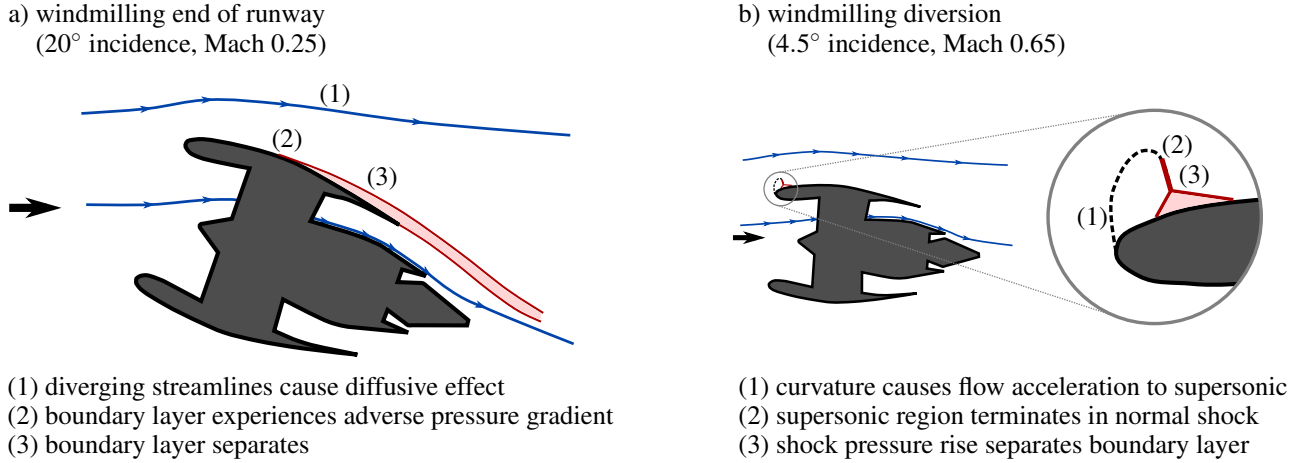


Figure 1: Schematic of flow separation mechanisms for a) end-of-runway windmilling and b) diversion windmilling.

Table 1: Operating conditions for the on-design cruise phase and the off-design windmilling scenarios.

case	height (m)	MFCR	FNPR	M_∞	α (deg)
cruise	10,700	MFCR _{cru}	FNPR _{cru}	0.85	4.5
end-of-runway windmilling	4600	MFCR _{EoR}	1.045	0.25	20
diversion windmilling	6100	MFCR _{div}	1.32	0.65	4.5

altitude, the mass flow capture ratio (MFCR, i.e. the ratio of the upstream streamtube capture area to the nacelle highlight area) and the fan nozzle pressure ratio (FNPR, i.e. the ratio of the total pressure at the nozzle inlet for the bypass stream to ambient static pressure). The altitude influences the local Reynolds number of the flow while the combined effect of α , FNPR and MCFR determines the stagnation point on the nacelle. These parameters are listed for each scenario in Table 1.

Importantly, the high angle of attack (20 degrees) in the Mach 0.25 end-of-runway case can cause separation by a subsonic diffusion mechanism (Fig. 1a). Meanwhile, the diversion scenario in Fig. 1b exhibits a very different flow field, where the severe nacelle lip curvature can accelerate the incoming Mach 0.65 flow to create a supersonic region – the normal shock which terminates this region can separate the boundary layer on the external surface.

In order to better define the flow problem, preliminary three-dimensional RANS computations are performed on a representative nacelle geometry. Whilst these computations may not capture all the flow physics entirely accurately, they are still thought to be instructive in guiding the design of the wind tunnel rig.

2.1 Representative nacelle geometry

The representative 3D non-axisymmetric baseline nacelle is designed for a long-range aircraft at $M_\infty = 0.85$ with a compact, dual separate jet exhaust. Appropriate values for the key nacelle dimensions are determined with a fully parametric definition that uses the intuitive class-

shape transformation (iCST) method [5, 6]. The design process is based on a multi-point, multi-objective optimisation routine based on a well-established CFD methodology [7, 8, 9, 10]. The mesh independence and validation of this numerical approach have been reported in a number of previous studies [8, 9, 11].

The initial Latin hypercube sampling (LHS) design space exploration uses 400 nacelle designs. Each design is assessed at six operating conditions, including the design cruise condition and both windmilling scenarios [12]. From this optimisation procedure, a 3D nacelle design is down-selected to minimise cruise drag whilst requiring that the length of any separation be less than 5% of the nacelle length, L_{nac} .

To better understand the flow fields, RANS simulations of both windmilling scenarios are performed for a range of operating conditions. This analysis is conducted at full-engine size with fully turbulent computations and the boundary layer is modelled using a wall function with freestream turbulence intensity of 0.1%. Based on the stated operating conditions, the Reynolds number based on lip thickness, Re_l , is estimated to be around 2.1×10^6 and 3.7×10^6 for the windmilling end-of-runway and diversion conditions, respectively.

2.2 End-of-runway windmilling

Under end-of-runway windmilling conditions ($M_\infty = 0.25$, $\alpha = 20^\circ$), Fig. 2 presents the isentropic Mach number, i.e. the Mach number defined by the local surface pressure, on an unwrapped view of half the fan cowl sur-

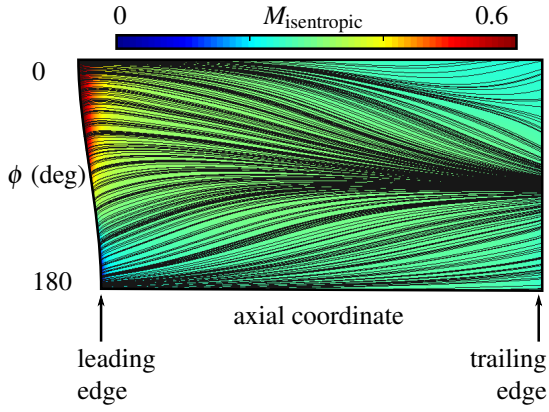


Figure 2: Isentropic Mach number and surface streamlines for end-of-runway windmilling.

face. This flow is subsonic and attached everywhere. Figure 3a indicates that at an increased incidence of 21° , however, there is a separated region on the nacelle which extends axially from the leading edge to about 80% of the nacelle length. This separation is azimuthally confined within the sector $0^\circ < \phi < 45^\circ$, where the azimuthal coordinate, ϕ goes from 0° at the upper lip to 180° on the lower lip.

Figure 3b presents the flow field for MCFR reduced in value by 15% from nominal end-of-runway windmilling conditions, with $\alpha = 20^\circ$. An abrupt separation appears on the nacelle between $0^\circ < \phi < 45^\circ$ from the highlight up to 90% of the nacelle length. Finally, when the FNPR is varied either side of its nominal value between 1.0 to 1.1, the flow over the fan cowl remains attached (Figs. 3c and 3d).

2.3 Diversion windmilling

Under windmilling diversion conditions, Fig. 4 indicates that the flow over the nacelle forebody is transonic, with a supersonic region terminating in a normal shock. The pre-shock Mach number is roughly 1.5, resulting in a closed separation which is azimuthally positioned around $\phi = 45^\circ$. In the axial direction, this separated region covers less than 5% of the nacelle length.

When the incoming Mach number is increased to 0.7, Fig. 5a shows that the shock moves downstream and increases in strength. As a result, the separation length increases slightly, although it remains shorter than 5% of the nacelle length. Meanwhile, reducing the freestream Mach number to 0.6 (Fig. 5b) causes the shock to move upstream such that it weakens, resulting in attached flow over the entire nacelle.

The flow field is also evaluated for a case with MCFR reduced by 11% in Fig. 5c. The shock location remains roughly constant but the peak pre-shock Mach number increases. Due to this enhanced shock strength, the extent

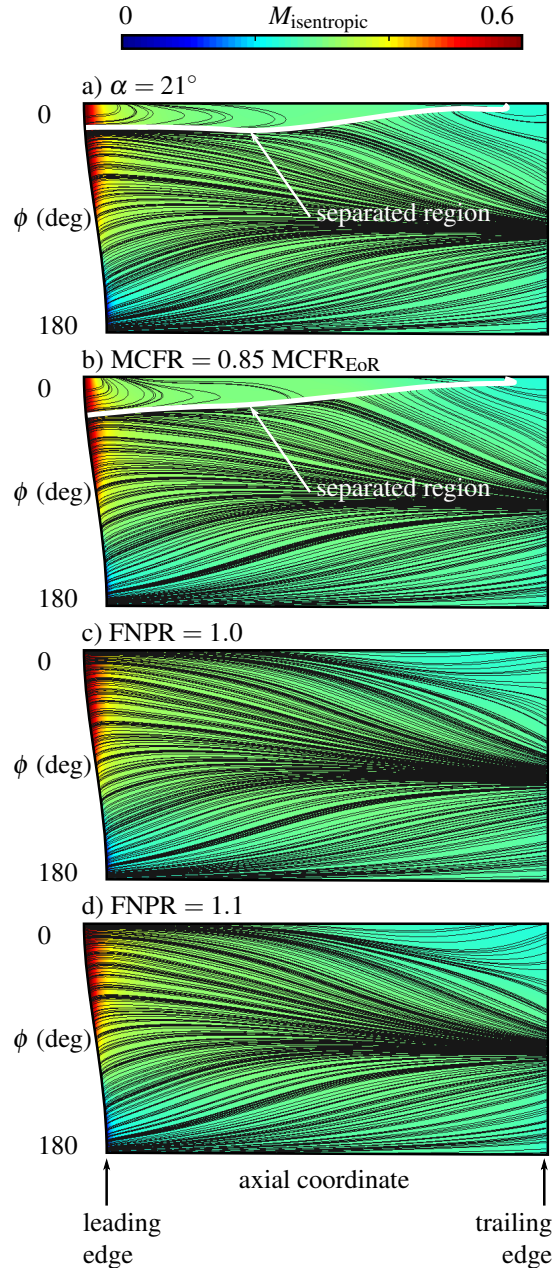


Figure 3: Isentropic Mach number and surface streamline pattern for end-of-runway windmilling with: a) increased incidence angle; b) reduced MCFR; c) reduced FNPR; and d) increased FNPR.

of the separation is increased to about 20% of the nacelle length. When the FNPR is varied from 1.15 to 1.35 (either side of the nominal value) in Figs. 5d and 5e, the flow over the fan cowl and the extent of the shock-induced separation remain roughly unchanged. Thus, the peak cowl Mach number (which varies between 1.4 and 1.6) and the shock strength both show a sensitivity to freestream Mach number and to MCFR but are insensitive to FNPR.

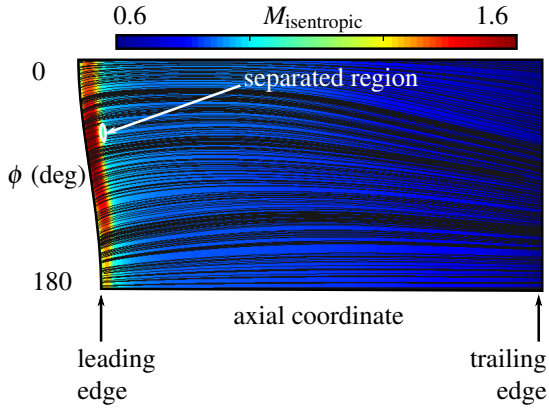


Figure 4: Isentropic Mach number and surface streamlines for diversion windmilling.

3. FROM ENGINE TO WIND TUNNEL

The experimental rig to investigate external fan cowl separation will be integrated into a blow-down transonic wind tunnel at the University of Cambridge. The wind-tunnel assembly, which is schematically depicted in Fig. 6 is fed from a high-pressure reservoir into the settling chamber, where it passes through a number of flow straighteners and turbulence grids, followed by an 18:1 contraction with a round-to-rectangular transition.

The test section, which is 114 mm wide and 1200 mm long, consists of an underlying tunnel structure, marked in light gray in Fig. 6, onto which custom-built liner blocks can be bolted. The sidewalls of the wind tunnel are formed by removeable doors containing two optical-access windows with 203 mm diameter, which are indicated in Fig. 6. The stagnation pressure can be set up to a maximum of 200 kPa, which permits some control over the Reynolds number of the flow in the test section.

A number of similar studies have been performed in the same facility previously to investigate the flow field around nacelle lips at high-incidence climb [13, 14] and in crossflow [15]. The overall test section architecture follows the same principles as these previous studies. In particular, Fig. 7 shows that the geometry of the constituent ceiling and floor liner blocks are based on a planar slice of 3D RANS simulations, with the liner contours matched to streamlines extracted from above and below the nacelle, respectively.

With this type of set-up, the angle of an airfoil downstream of the test section (shown in Fig. 6) can be set to change the effective area of a “rear throat”, where the flow is choked. The area ratio between this rear throat and the test-section inlet determines the entry Mach number.

The nacelle model in Fig. 7 splits the test section flow into two channels. This two-channel set-up permits control over the mass flow capture ratio. By controlling the effective flow area in this region, a choking rod sets the

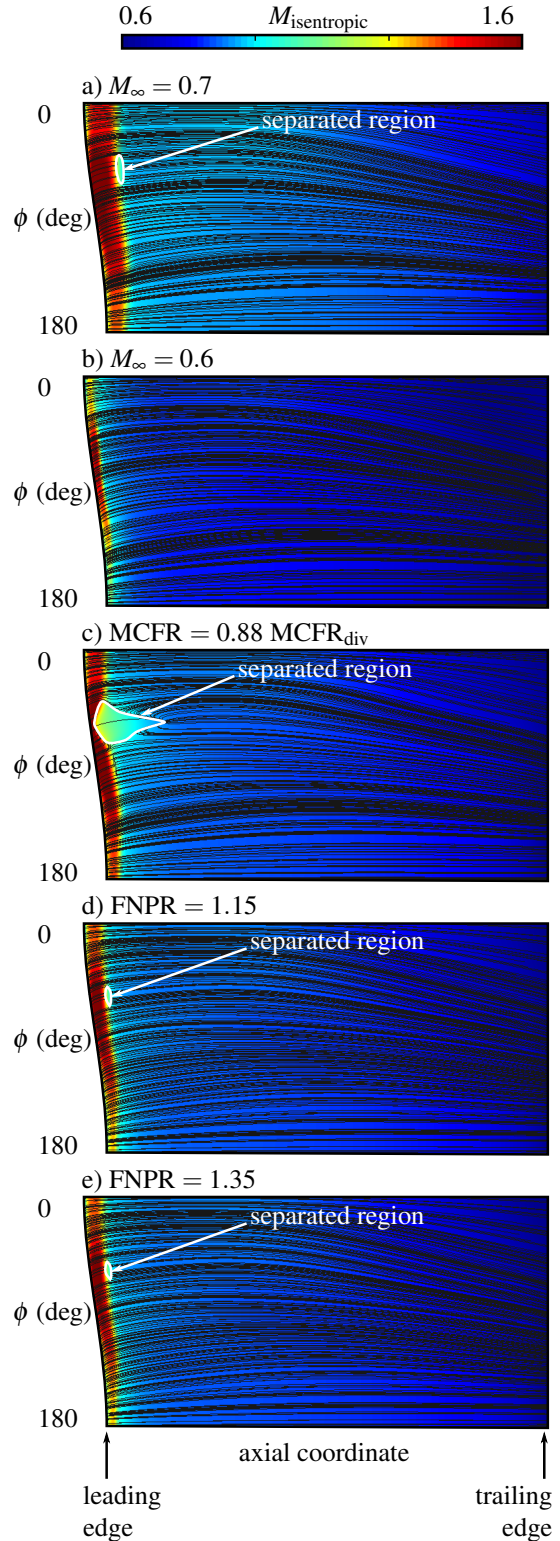


Figure 5: Isentropic Mach number and surface streamline pattern for diversion windmilling with: a) increased Mach number; b) reduced Mach number; c) reduced MCFR; d) reduced FNPR; and e) increased FNPR.

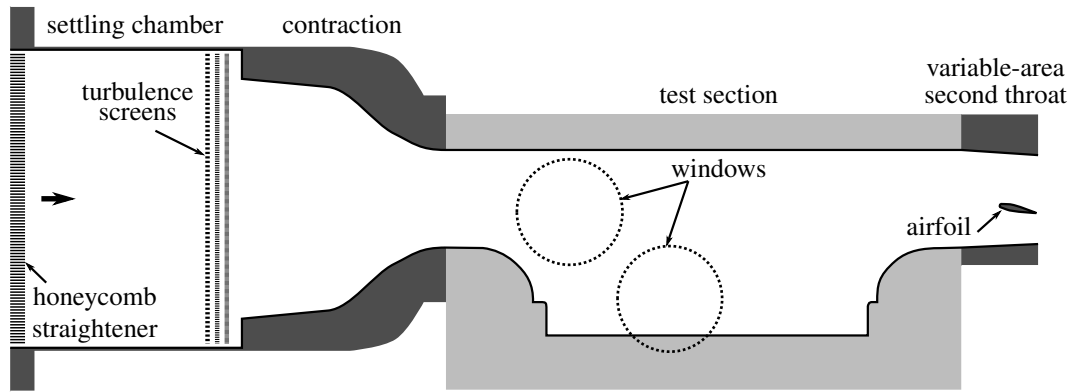


Figure 6: Schematic of the wind tunnel facility into which the nacelle rig is integrated.

mass flow in through the internal inlet channel. As a result, this set-up allows control of the mass flow split between the two channels, thereby allowing different values of MCFR to be tested.

Therefore, the test section concept in Fig. 7 can replicate the flow fields for the end-of-runway and diversion windmilling scenarios. The rig provides control over the key parameters of entry Mach number, Reynolds number, and mass flow capture ratio. However, to ensure that the salient flow physics are captured, the design process requires more careful thought than simply extracting arbitrary bounding streamlines from the 3D simulations and inserting these into the existing wind tunnel structure, as detailed in the following section.

4. DETAILED RIG DESIGN

In order that the wind tunnel experiments replicate the desired flow physics, it is important to consider a number of important questions:

- What is the appropriate size for the nacelle model?
- Since the liner blocks need to remain fixed, how far away do the bounding streamlines need to be to be unperturbed as the flow field changes?
- Over what Reynolds number range can the flow physics be expected to remain unchanged?
- How do the bounding streamlines interface with the existing tunnel structure in terms of geometry continuity?
- How should the bounding streamlines be adjusted to account for the differences between two- and three-dimensional flow fields?
- What are the effects of the tunnel wall boundary layers and how should these be taken into account?

Existing 3D RANS computations of the full engine are used alongside 2D computations of the wind tunnel flow path to address these questions.

The 2D RANS simulations of the wind tunnel use a double-precision density-based solver with an implicit

time-integration formulation. The computation of the numerical fluxes is based on a Roe scheme with the Green–Gauss method for spatial discretisation and $k - \omega$ shear-stress transport is used for turbulence modelling [16]. The CFD domain, presented in Fig. 8, encompasses the nacelle aeroline and the bounding streamlines which are modelled as viscous adiabatic walls. The bounding streamlines are axially extruded at the inlet and outlet by about twice the rig inlet height to improve numerical stability. Total pressure and static pressure boundary conditions are imposed at the domain inlet and outlet, respectively. At the outlet a target mass flow is prescribed to achieve the desired inlet Mach number. To replicate the choking rod used to control the mass flow split between the two channels and change the position of the stagnation point, a dynamic head loss is prescribed at a porous region located at about 70% of the nacelle length (Fig. 8).

The mesh is fully structured with near-wall resolution, $y^+ \approx 1$, and a mesh independence study is performed for no head loss through the porous region [17]. Three levels of mesh refinement are generated whose overall size was 4.3×10^4 , 6.5×10^4 , and 1.1×10^5 nodes. The medium of these three meshes (Fig. 8) is considered to be sufficiently mesh independent with a grid-convergence index of 0.04% when applied to peak isentropic Mach number.

The diversion windmilling scenario is used as a representative example to illustrate the key design considerations, with a similar procedure conducted separately for the end-of-runway case.

4.1 Scaling of the nacelle model

Selecting the correct size of nacelle model in this relatively small-scale facility requires a delicate balance. If the model were too small, the Reynolds number would be much smaller than that encountered in flight scenarios and so the studied flow field may exhibit quite different behaviour. In addition, any physical flow features such as boundary layers or separated regions would be correspondingly smaller in scale and so may be difficult

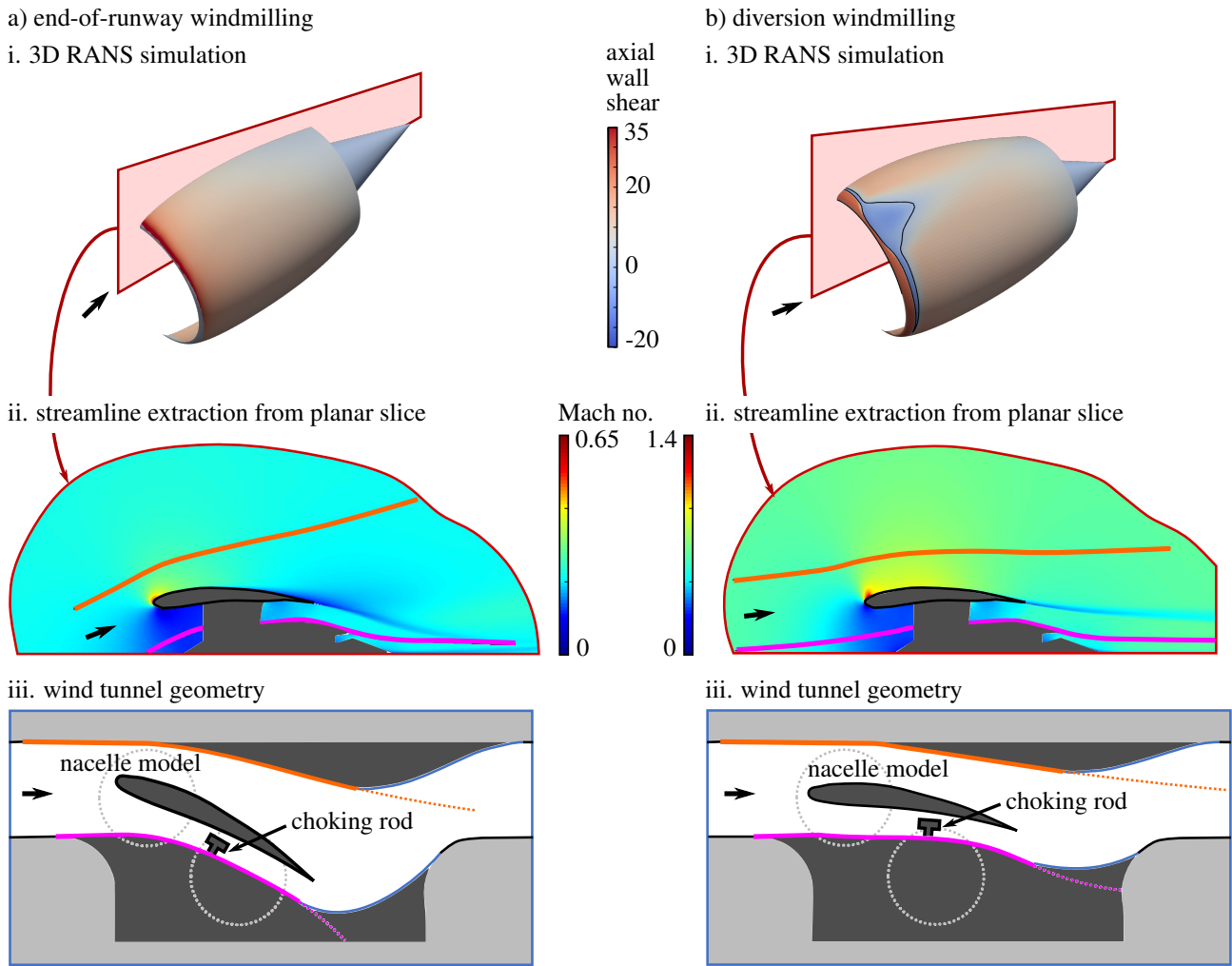


Figure 7: Schematic generation of the wind tunnel geometry for a) end-of-runway windmilling and b) diversion windmilling: i. 3D RANS simulations of the entire nacelle; ii. streamlines from a slice through the vertical plane; iii. the wind tunnel geometry with wall contours defined by extracted streamlines.

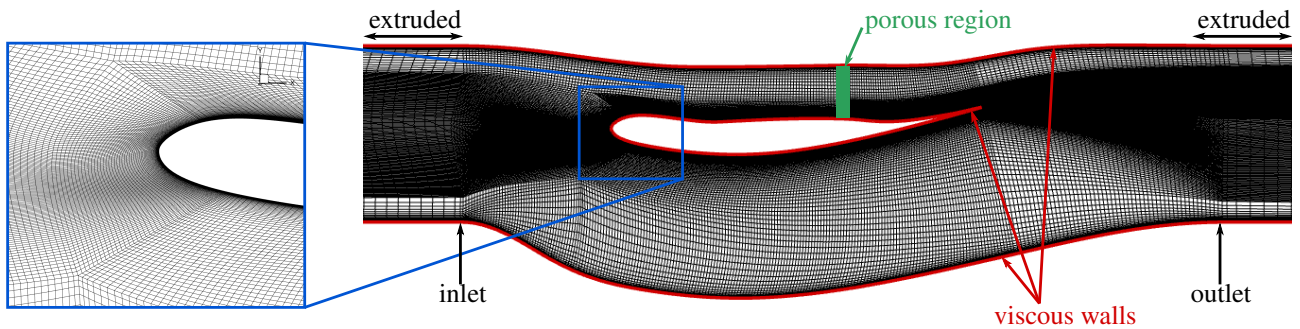


Figure 8: Mesh for 2D computations of the wind tunnel flow path.

to measure accurately.

On the other hand, if the nacelle model were too large, the bounding streamlines formed by the liner blocks would be very close to the nacelle surface in relative terms. As the flow behaviour on a full-scale nacelle changes with an adjustment in some operating condition,

streamlines close to the nacelle surface are perturbed. In contrast, the contours of the tunnel liner blocks are fixed and so their inability to accommodate such streamline changes would likely cause significant wall effects if the liners are located too close to the model.

In order to determine a suitable scale for the model, it is

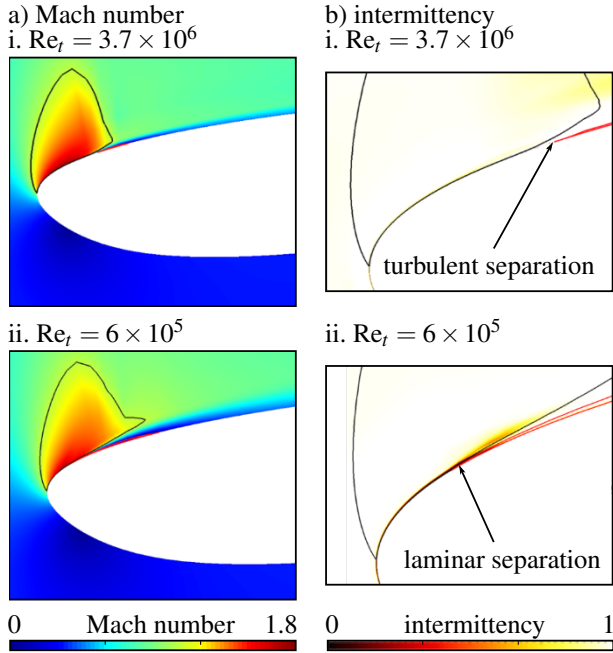


Figure 9: Transitional boundary-layer computations for diversion windmilling with $MCFR = 0.89 MCFR_{div}$ showing a) Mach number and b) intermittency (0: laminar, 1: turbulent): i. $Re_t = 3.7 \times 10^6$ and ii. $Re_t = 6 \times 10^5$.

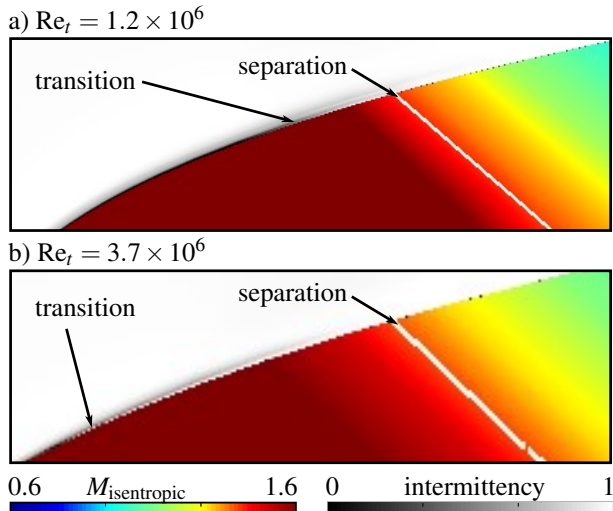


Figure 10: Transitional computations for diversion windmilling in $\phi = 60^\circ$ plane with $MCFR = 0.89 MCFR_{div}$ at a) $Re_t = 1.2 \times 10^6$ and b) $Re_t = 3.7 \times 10^6$.

therefore essential to balance: (i) the minimum Reynolds number at which a wind tunnel experiment replicates the flow physics of the full-scale engine, with (ii) how close bounding streamlines can be to the model whilst remaining roughly unperturbed across the regimes of interest. The three-dimensional RANS simulations of the entire engine are used to evaluate this balance.

Effect of Reynolds number On a full-scale engine the Reynolds number based on the lip thickness, $Re_t \approx 3.1 - 3.7 \times 10^6$, but this cannot be achieved in the experimental rig. For a maximum total pressure of 200 kPa, the wind tunnel rig can achieve approximately $Re_t \approx 6 \times 10^5$ if the nacelle model is at 1/30th scale.

Computations of the entire nacelle are performed using the $\gamma - Re_\theta$ boundary-layer transitional model at the full-scale Reynolds number of 3.7×10^6 and the lower “rig-relevant” value of $Re_t = 6 \times 10^5$. These computations, shown in Fig. 9, exhibit distinct shock-induced separation mechanisms in the two cases. At the higher Reynolds number, Fig. 9a shows that the incoming boundary layer which encounters the shock wave is turbulent. On the other hand, the lower Reynolds number exhibits a laminar separation, with a subsequent transition to turbulence followed by flow reattachment (Fig. 9b). Given this sensitivity to Reynolds number, a 1/30th scale nacelle is not suitable and so a larger-scale model is required to produce a turbulent (rather than laminar or transitional) shock-boundary-layer interaction.

An analysis of the state of the pre-shock boundary layer at a slightly higher “rig-relevant” Reynolds number, $Re_t = 1.2 \times 10^6$, in Fig. 10 suggests that transition occurs a few boundary-layer thicknesses upstream of the shock wave and therefore the interaction is likely turbulent in nature. This Reynolds number corresponds to a nacelle at 1/14th scale and so this sets the minimum model size.

Choice of bounding streamlines Plausible bounding streamlines are considered in Fig. 11 for two different values of MCFR. Even though the size of separation increases considerably in size as the MCFR is reduced by 11% (Figs. 4 and 5c), the contours of the selected bounding streamlines remain almost identical. Therefore, whilst more ambitious bounding streamlines closer to the nacelle surface may also be acceptable, the highlighted streamlines in Fig. 11 are not expected to experience significant tunnel wall effects.

4.2 Further design considerations

Once the scale of the nacelle model has been defined, it is necessary to integrate this geometry into the existing wind tunnel structure whilst considering the optical access requirements, the 2D nature of the facility, and the tunnel boundary layers.

Integration into tunnel structure In Fig. 7, the streamlines extracted from the computations are blended with the existing tunnel structure whilst maintaining gradient and curvature continuity in the geometry contours. Figure 12 shows that achieving this type of integration can be achieved much more easily by inverting the geometry, such that the upper-bounding contour is repre-

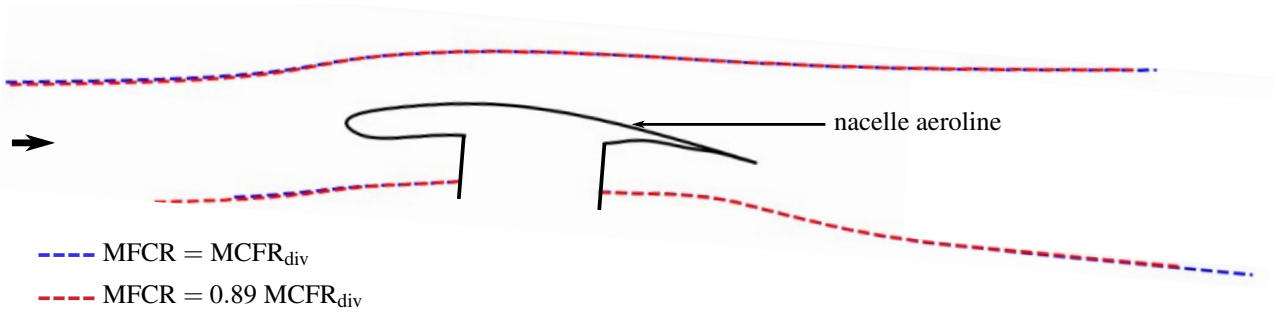


Figure 11: Sensitivity of the bounding streamline shape on MFCR for diversion windmilling.

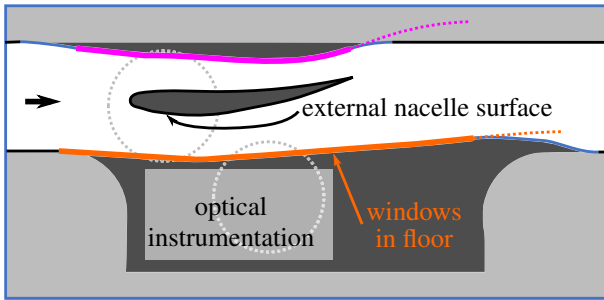
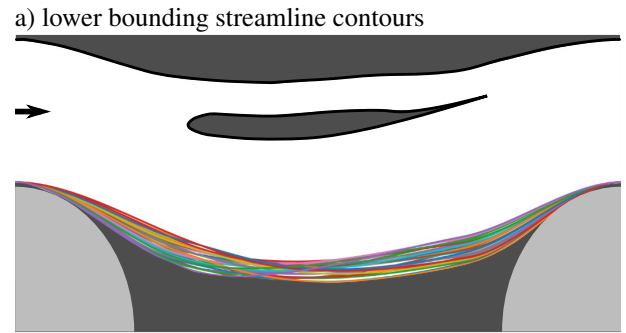


Figure 12: Schematic tunnel setup with inverted nacelle.

representative of a streamline that is captured within the engine whereas the lower-bounding streamline belongs to the region external to the nacelle. Such an arrangement also reduces the required curvature of the liner blocks, thereby reducing the likelihood of problems associated with tunnel wall separation or undesired supersonic regions.

Optical access requirements It is essential that the nacelle lip be centred on one of the optical access windows to ensure that the flow field in this region can be studied using schlieren visualisation and optical velocimetry methods. Fig. 12 satisfies this requirement but also provides another advantage in terms of the optical access. The inverted setup contains considerable empty space in the bottom liner block (Fig. 12). Windows can be installed into this floor surface, which would allow instrumentation such as light sources and cameras to be targeted at the external nacelle surface. This optical setup would be particularly beneficial for techniques such as oil-flow visualisation and pressure-sensitive paint by providing flow information over the entire nacelle length which could not be obtained from the sidewall windows alone.

2D versus 3D geometries Consider a streamtube in the three-dimensional computations which grows such that the contained area is doubled between two streamwise locations. If the same streamtube were implemented in



a) lower bounding streamline contours

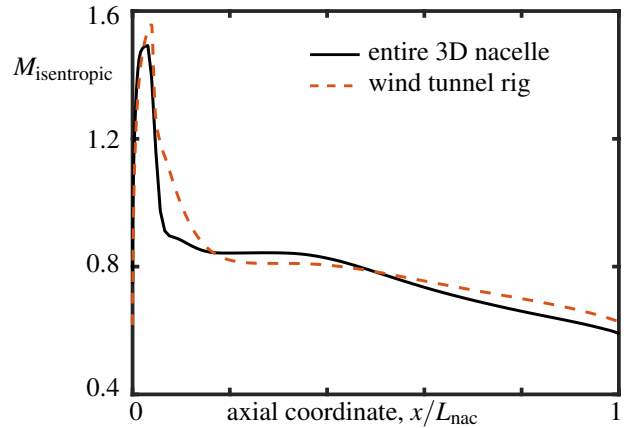


Figure 13: a) Lower bounding streamline contours, including additional pressure relief to account for wind tunnel being quasi-2D. b) Mach number distribution for selected contour.

a two-dimensional wind tunnel, the flow area would not double but would only increase by a factor of $\sqrt{2}$, since the spanwise dimension remains constant. As a result, exactly the same streamline contour would not replicate the original flow area profile, and so the true Mach number distribution would not be recovered. In order to account for this difference, it is necessary to perturb the bounding streamlines to reproduce the Mach number variations from the 3D flow field.

To achieve this, the lower bounding streamline is ad-

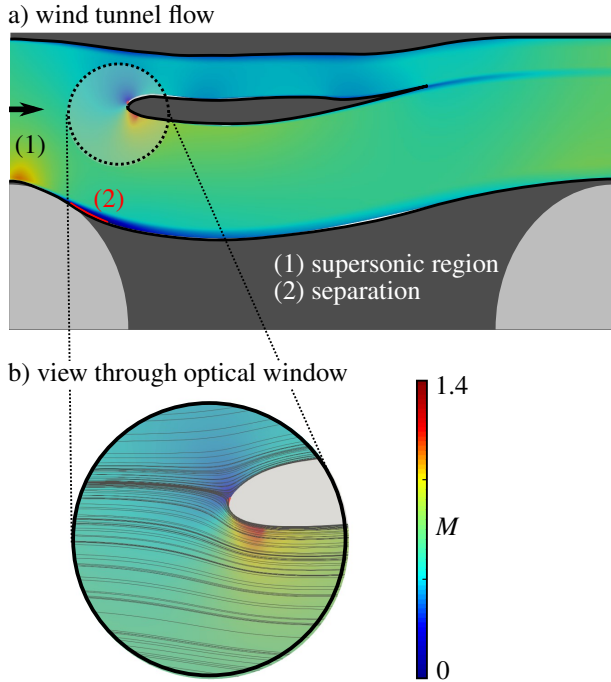


Figure 14: Mach number distribution for selected geometry a) over entire flow path, and b) within optical window.

justed by conducting an initial Latin Hypercube Sampling (LHS) with 25 samples (Fig. 13). In particular, the lower bounding streamline follows a fully parametric description based on iCST [5] to finely control the lower channel area distribution. Overall, three iCST curves are defined, the first and last of which blend the streamline to the rig end points. The central iCST is defined through four geometric parameters that change the shape of the bounding streamline and thus control the flow acceleration along the nacelle forebody. Figure 13 shows that, even with a relatively small number of samples, the required Mach number profile can be recovered accurately.

Ongoing work The geometry in Fig. 14 appears to accurately reproduce the physical flow field. However, the nacelle lip is located at the downstream end of the optical window so post-shock boundary-layer measurements are somewhat restricted. In addition, the substantial curvature at the start of the bottom liner contour produces two undesirable effects – a supersonic region, labelled (1) in Fig. 14, as well as a separated shear layer, marked (2) in the figure. In order to address these limitations, the LHS method is being further developed to achieve the target local aerodynamics. As part of this process, the nacelle position is constrained to the windows and the liner geometry curvature is limited.

The Reynolds-number analysis in Section 4.1 suggests that nacelle models which are at least 1/14th scale should correctly replicate the turbulent interaction observed in the full-scale computations. However, it is also necessary

to perform a similar analysis at the tunnel total pressure and a higher total pressure (representative of full-scale Reynolds number conditions) to ensure that the rig does indeed reproduce the expected turbulent interaction.

Since the 2D computations of the wind tunnel define no-slip boundary conditions on the floor and the ceiling, the inverse design process accounts for the boundary layers developing along these surfaces. However, the computations do not account for the boundary layers on the sidewalls which, as they develop, influence the effective flow area. Three-dimensional computations of the wind tunnel flow, including the sidewalls, allow these effects to be quantified and for the liner block geometry to be subsequently adjusted to account for them.

5. CONCLUSIONS

This paper presents the design process for a new transonic wind tunnel rig to investigate separation on the external surface on the upper nacelle lip of ultra-high bypass ratio engines in two off-design conditions. End-of-runway windmilling conditions, experienced during take-off climb out, feature low Mach numbers ($M = 0.25$) and high angles of attack ($\alpha = 20^\circ$), causing external fan cowl separation through subsonic diffusion. Meanwhile, the higher Mach number ($M = 0.65$) and lower angle of attack ($\alpha = 4.5^\circ$) in windmilling diversion, for engine shutdown during cruise, exhibits a supersonic region around the lip and normal shock-induced separation.

Separation in these scenarios is particularly relevant to UHBR nacelles, which tend to feature more aggressive curvature compared to traditional engine fan cowl geometries. In both scenarios, the prohibitive drag penalty when separation occurs motivates the need to better understand its onset and underlying physical mechanisms.

In order to replicate the flow around a real nacelle in a wind tunnel, streamlines are extracted from a planar slice through 3D RANS computations of a representative nacelle geometry. These streamlines, which define the floor and ceiling of the wind tunnel flow path, are blended into the existing tunnel geometry. The exact contours of the bounding streamlines are adjusted using an inverse-design process to account for the 2D nature of the wind tunnel as well as the presence of wall boundary layers.

To prevent tunnel wall effects from influencing the flow around the nacelle, bounding streamlines sufficiently far away from the model surface are selected for the linear block contours. Whilst the limited total pressure in the wind tunnel prevents the Reynolds number in the real nacelle ($Re_t \approx 3.7 \times 10^6$) from being exactly replicated, the nacelle model is designed to be at least 1/14th scale ($Re_t = 1.2 \times 10^6$), which is sufficient to reproduce the turbulent shock–boundary-layer interaction observed at full scale.

Therefore, the designed wind tunnel rig faithfully rep-

resents the flow conditions experienced by real nacelles in end-of-runway and diversion windmilling scenarios. In this rig, a number of optical measurement techniques – schlieren visualisation, laser Doppler velocimetry, surface oil-flow visualisation, and pressure sensitive paint – will enable the flow field on the external nacelle surface to be probed. The data collected in this rig will provide valuable insight into the fundamental flow physics governing the onset of and physical mechanisms relating to separation in these off-design situations. In addition, by validating RANS and higher-fidelity computations of the wind tunnel flow, relevant numerical techniques will be further developed. In this way, the current study will provide valuable information for aircraft and engine manufacturers so that they can design nacelles for low-emission engines which will exhibit optimal aerodynamic performance even in off-design conditions.

ACKNOWLEDGEMENTS

This project has received funding from the Clean Sky 2 Joint Undertaking (JU) under grant agreement No 101007598. The JU receives support from the European Union’s Horizon 2020 research and innovation programme and the Clean Sky 2 JU members other than the Union.

REFERENCES

- [1] European Commission. FlightPath 2050: Europe’s vision for aviation. Technical Report EUR 098 EN, Publications Office of the European Union, 2011.
- [2] C. Hughes. The promise and challenges of ultra high bypass ratio engine technology and integration. Technical report, National Aeronautics and Space Administration, 2011.
- [3] A. Magrini, E. Benini, H.-D. Yao, J. Postma, and C. Sheaf. A review of installation effects of ultra-high bypass ratio engines. *Progress in Aerospace Sciences*, 119:100680, 2020.
- [4] W. Hoelmer, J.L. Younghans, and J.C. Raynal. Effect of Reynolds number on upper cowl flow separation. *Journal of Aircraft*, 24(3):161–169, 1987.
- [5] R. Christie, A. Heidebrecht, and D. MacManus. An automated approach to nacelle parameterization using intuitive class shape transformation curves. *Journal of Engineering for Gas Turbines and Power*, 139(6), 2017.
- [6] R. Christie, M. Robinson, F. Tejero, and D.G. MacManus. The use of hybrid intuitive class shape transformation curves in aerodynamic design. *Aerospace Science and Technology*, 95:105473, 2019.
- [7] F. Tejero, D.G. MacManus, and C. Sheaf. Surrogate-based aerodynamic optimisation of compact nacelle aero-engines. *Aerospace Science and Technology*, 93:105207, 2019.
- [8] F. Tejero, M. Robinson, D.G. MacManus, and C. Sheaf. Multi-objective optimisation of short nacelles for high bypass ratio engines. *Aerospace Science and Technology*, 91:410–421, 2019.
- [9] M. Robinson, D.G. MacManus, R. Christie, C. Sheaf, and N. Grech. Nacelle design for ultra-high bypass ratio engines with cfd based optimisation. *Aerospace Science and Technology*, 113:106191, 2021.
- [10] F. Tejero, R. Christie, D. MacManus, and C. Sheaf. Non-axisymmetric aero-engine nacelle design by surrogate-based methods. *Aerospace Science and Technology*, page 106890, 2021.
- [11] M.H. Robinson, D.G. MacManus, K. Richards, and C. Sheaf. Short and slim nacelle design for ultra-high bpr engines. In *55th AIAA Aerospace Sciences Meeting*, 2017–0707.
- [12] B.J. Deneys Schreiner, F. Tejero, D.G. MacManus, and C. Sheaf. Robust aerodynamic design of nacelles for future civil aero-engines. In *Turbo Expo: Power for Land, Sea, and Air*, volume 84058, page V001T01A015. American Society of Mechanical Engineers, 2020.
- [13] A. Coschignano, H. Babinsky, C. Sheaf, and G. Zamboni. Normal-shock/boundary-layer interactions in transonic intakes at high incidence. *AIAA Journal*, 57(7):2867–2880, 2019.
- [14] C.E. O’Pray, H. Babinsky, and C. Sheaf. The influence of surface geometry on the fan-plane boundary-layer in transonic intakes at high-incidence. In *AIAA Scitech 2022 Forum*, 2022–1806.
- [15] L. Dickinson, H. Babinsky, and C. Sheaf. Crosswind-induced shockwave-boundary-layer interactions in subsonic inlets. In *56th 3AF International Conference on Applied Aerodynamics*, FP07–2022.
- [16] F.R. Menter. Improved two-equation k-omega turbulence models for aerodynamic flows. Technical report, National Aeronautics and Space Administration, 1992.
- [17] I.B. Celik, U. Ghia, P.J. Roache, and C.J. Freitas. Procedure for estimation and reporting of uncertainty due to discretization in CFD applications. *Journal of Fluids Engineering - Transactions of the ASME*, 130(7), 2008.